A Revised Inductance Distribution Analysis of Medium-Large Caliber Electromagnetic Launchers including a Large Bus Structure

Nail Tosun,[1, a)] Görkem Gülletutan,[1] Anıl Civil,[2] Ahmet Yasin Oruç,[2] Baran Yıldırım,[2] Bekir Mert Özceylan,[2] Emre Burak Yurdakul,[2] Evren Tan,[2] Ferhat Yurdakonar,[2] Hüseyin Akdemir,[2] İbrahim Güngen,[2] Mustafa Karagöz,[2] Özgur Cavbozar,[2] Rasih Hakan Demirkol,[2] Ulaş Göçmen,[2] and Ozan Keysan[*,1]

[1)]*METU Powerlab, Department of Electrical and Electronics Engineering, Middle East Technical University*
[2)]*Defence System Technologies Business Sector, ASELSAN Inc.*

(*The author to whom correspondence may be addressed: keysan@metu.edu.tr)

(Dated: 17 February 2023)

An important application for large-scale pulse power supplies (PPS) is electromagnetic launchers (EMLs). These devices utilized stored several MJs of electrochemical energy into linear mechanical energy. Because of extreme physical conditions, simulations are crucial in electromagnetic launcher (EML) research. As the operation risk rises, more energy into the system adds weight to the model's accuracy. In this paper, the electromagnetic impact of the bus structure is discovered in a recently developed EMFY-3 electromagnetic launcher, is presented. An H-shaped bus structure is used for the current injection. However, experiments showed that the H-shaped bus changes inductance calculations. A careful examination is made to reveal the physical reasoning behind the bus impact. We hypothesize that the rail portion surrounded with bus geometry has less inductance than the rest due to the eddy current created by rail current transients, which should be calculated carefully through numerical calculations, i.e., 3-D Finite Element Method (FEM). Two different simulation models were constructed to test the hypothesis. Moreover, rail currents, breech, and muzzle voltages are measured to investigate electromagnetic calculations. Results showed a good agreement with experiments where the bus structure was modeled explicitly. That aspect showed that the bus structure should be well-examined when multiple PPS are connected.

I. INTRODUCTION

At ASELSAN Inc., electromagnetic launchers (EMLs) are examined since 2014. ASELSAN's most powerful EML, EMFY-3, reached 2.91 MJ muzzle energy, at 36% efficiency, with an 8 MJ pulse power supply (PPS) in the ASELSAN's Electromagnetic Launch Laboratory. These experiments are demonstrated in the previous article[1]. EMFY-3 launcher is illustrated in Fig. 1, and geometric parameters are in Table I. 4 MJ PPS segment is presented in Fig. 2.

Multiple capacitor-based modules are combined to provide an 8 MJ input electrical energy. In order to give a reference for these parameters, a 200 kJ capacitive-based PPS[2] is used. Values are listed in Table II. Each unit's triggering time influences the rail current waveform. A flat-top rail current is desirable to reduce eddy current losses, inductive voltage oscillations, and preferable contact forces. The relationship between the rail current waveform and the set of triggering times should be programmable to operate EML properly. Some studies use evolutionary algorithms (EA) to evaluate triggering times, considering the relationship is non-programmable. However, as Zhang *et. al.* stated that for a given magnitude of flat rail current, the set of triggering time is unique and can be calculated iteratively[3,4]. Additionally, we assessed the range of triggering timings using an iterative method while taking the shape of the rail current and targeted muzzle velocity into account[5]. It should be recognized, nonetheless, that all these calculations strongly rely on the model's accuracy.

Compared to PPS circuity, the EML's electromagnetic modelling presents a variety of difficulties. For instance, EML's inductance and resistance are dynamic physical properties. The armature's position and speed, the electrical excitation frequency, and complex contact states all have an impact on them. The accuracy and the minimum computational burden are two contradicting objectives. The literature contains numerous attempts to improve the simulation accuracy of EMLs. They can be classified into three: lumped circuit method (LCM), Finite Element Method (FEM), and FEM-assisted lumped circuit method.

LCMs are constructed with some dynamic circuit elements, i.e., resistance and inductance gradients related to launching dynamics[6–8]. Dynamic parameters can be calculated analytically, or they can be extracted from numerical tools. The simulation model has one dimension, so the strategy has the least computational effort.

TABLE I. Geometric Parameters of the Launcher.

Rail Height	50 mm
Rail Separation	75 mm
Rail Length	6.1 m

FEM prefers to solve complete EML geometry in the electromagnetic FEM. Such a method requires a significant investment in computation due to the high aspect ratio (thin-long rails) of EMLs. Additionally, commercial FEM tools are unable to model 3-D sliding contacts[11]; therefore, special FEM codes[12–14] are needed.

The FEM-assisted lumped circuit approach might be referred to as a hybrid method because it is a compromise position between LCM and FEM. For instance, a co-simulated

EMFY-1   EMFY-2   EMFY-3

2019   2020   2021

Muzzle energy

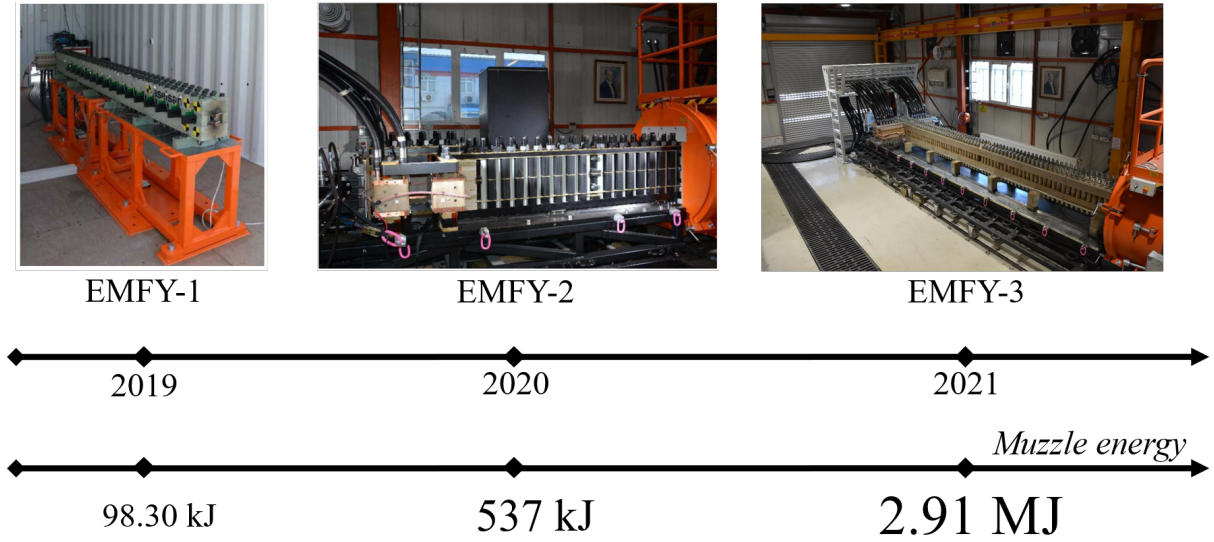98.30 kJ   537 kJ   2.91 MJ

FIG. 1. Three generations of EMFY launchers; EMFY-1, EMFY-2, and EMFY-3[9].

FIG. 2. 4 MJ PPS segment.[10]. Two of them are utilized to achieve 8 MJ.

TABLE II. Parameters of a 200 kJ capacitive-PPS[2].

	Description	Value
C	Capacitance of the capacitor bank	4 mF
R_C	ESR of the capacitor bank	0.25 mΩ
L_C	ESL of the capacitor bank	0.1 μH
R_D	ON resistance of the crossbar diode stack	0.6 mΩ
L_{PPS}	Inductance of the pulse shaping inductor	20 μH
R_{PPS}	ESR of the pulse shaping inductor	0.1 mΩ
R_T	ON Resistance of the thyristor stack	0.1 mΩ
R_{Cable}	Cable resistance	0.9 mΩ
L_{Cable}	ESL of the cable	0.44 μH

LCM that accounts for the influence of movement might reduce the computational load of FEM.[15–17].

We carried out the EMFY-3 experiments, but there are some discrepancies with the simulations. Rail currents are overestimated, particularly in the beginning, which causes higher experimental peak currents. Given that EML is only capable of a maximum linear current density, it is hazardous to underestimate peak current[18,19]. Investigations lead us to the conclusion that the bus geometry is to reason for the mismatches. When the rail current changes, this conductive structure blocks the magnetic field change of the rail. As the magnetic field can not diffuse due to bus' eddy currents, the rail portion inside to bus structure has less inductance. Since the initial model does not consider this effect, the barrel's inductance is overestimated, concluding less rail current than actual values at the initial stages. This effect is different in magnitude at previous prototypes, EMFY-1 and EMFY-2 launchers. It is understood that medium to large-caliber EMLs suffer more from the bus impact since the bus structure becomes bulkier. Thus, it is crucial to add this inductance to the calculation, otherwise, the peak rail current can reach values that carry operational risks. Moreover, the reduction in the inductance can create another operational risk. The armature may stall at the end since the incremental inductance is reduced.

This study introduces a new EML modeling strategy enhanced with the bus' inductance effect. 3-D Finite Element Method (FEM) models are used to calculate bus inductance, propulsive inductance gradient L'_{pr}, or other characteristic parameters. These parameters are imported to the 1-D model to compare with experimental findings. Moreover, a control method where the bus impact is excluded is proposed to investigate its influence. The study revealed that the bus structure substantially influences the system's inductance, where estimations of peak rail currents and muzzle energies were improved by 5.71% and 2.40% on average, respectively.

II.   SIMULATIONS MODELS

Simulations are essential for the design and analysis procedure of EML as they operate in extreme physical conditions;

a few MA current excitations, several hundred MPa rail pressures, material phase changes, etc. Moreover, the electromagnetic analysis of EML is a challenging topic, as there is no consensus on the methodology. The 3-D FEM is an excellent choice as the calculations are geometry-dependent; however, electromagnetic formulations in 3-D FEM have limitations due to sliding electrical contact. EML strategies are illustrated in Fig. 3. This paper constructs a model using the LCM approach due to its simplicity and computational efficiency. However, model parameters are estimated using 3-D FEM simulations.

In this section, the main focus is to investigate bus geometry's influence on EML. In this regard, two simulation models are built; the control method and the proposed method. The proposed method takes into bus's inductance, unlike the control method. As these models differ at a single point, the control method creates a reference level to investigate the phenomena.
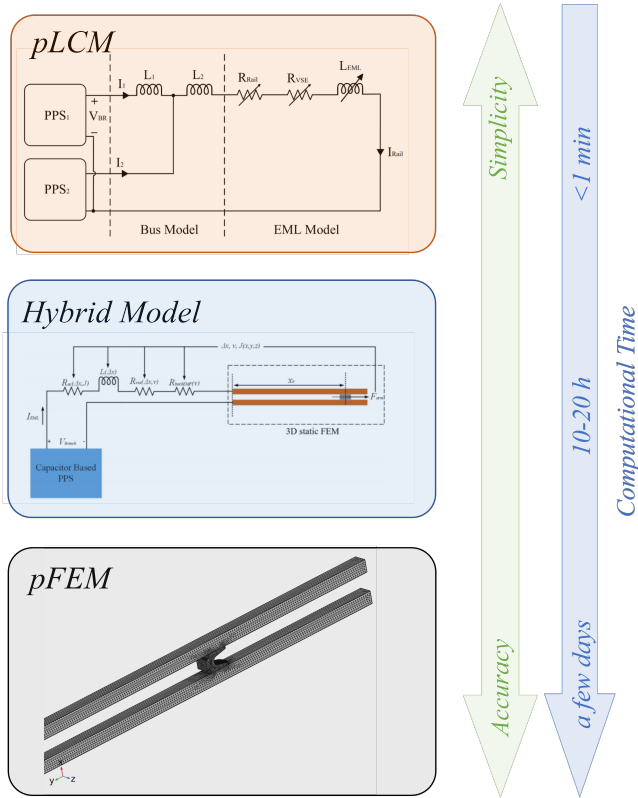

FIG. 3. EML simulation strategies.

To prevent rail displacements caused by EM stresses, high-mechanical strength containment is placed around the rails. Rails are mechanically rigid and static as a result. If there is even a small amount of rail displacement during the launch, there is a significant chance that the contact between the rails and the armature would break, endangering the operation. Thus the containment can be modeled as air, if the containment is non-conductive[20–22] and rails are considered as rigid, static bodies. However, it should be noted that the current density distribution inside the rails is changing throughout the
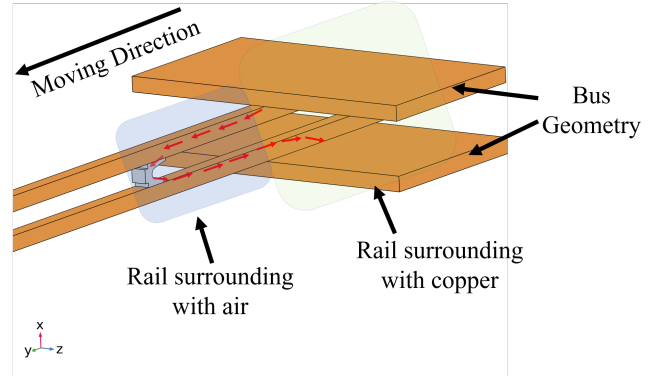

FIG. 4. The bus impact phenomenon. Red arrows indicate the current direction. The moving direction of the armature is specified as well. Two regions are illustrated with respect to inductance regions with colors. The blue region is surrounded with air, whereas the green region is enclosed by bus geometry. As the bus is conductive, the green region's magnetic field distribution is affected by eddy currents at the bus.

launch. This is because the conductor size is much larger than the wavelength of the excitation, and the diffusion process alters the current distribution. This dynamic inductance contribution is added to the calculation by using a dynamic L_{int} term.

When the bus geometry is close to the rails and covers a significant portion, it is essential to cover this geometry. Due to eddy currents, the bus is connected with rails, and the magnetic field density distribution is disturbed. Thus these two regions' inductance should be modeled individually, not from a single parameter, i.e., L'. This eddy current effect is called bus impact. This phenomenon is illustrated in Fig. 4.

From the electrical point of view, an EML can be expressed as series-connected variable resistance and inductance as in Fig. 5. The launcher's inductance depends on the armature's position; its resistance depends on both the position and velocity of the armature as the velocity skin effect (VSE) should be considered, which requires mechanical states to be calculated continuously.
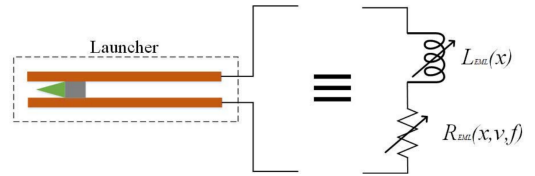

FIG. 5. Electromagnetic launcher can be modeled as a series connected variable resistance and inductance.

The control method is the simulation model used before the experiments; thus, it excludes the phenomenon. On the other hand, the proposed method includes bus' inductance, which helps to increase the model's accuracy. These two models also have common points, i.e., they use the same kine-mechanical calculations. Thus, these points are explained first, then the

differences are explained in the following subsections in detail.

A.   Common Features

1.   EML Modeling

The electromagnetic launcher can be considered a one turn coil with a time-dependent inductance.

$$\Phi(t) = \lambda(t) = L(t)I(t) \tag{1}$$

The electromotive force (EMF) can be calculated using Lenz's Law.

$$\varepsilon(t) = \frac{d\lambda(t)}{dt} = \frac{dL(t)}{dt}I(t) + L(t)\frac{dI(t)}{dt} \tag{2}$$

The second term in (2) is the voltage induced due to rail current transients. As EML inductance increases with the armature movement, as shown in (3). The inductance gradient can be calculated with 3-D FE, using the flux-counting method as demonstrated in[16].

$$L(t) = L'\Delta x(t) \tag{3}$$

The rail resistance variation can be calculated similarly as in (4). However, (4) does not reflect the velocity skin effect (VSE), a dominant phenomenon where armature velocity exceeds 500 m/s. VSE resistance, R_{vse}, due to current diffusion in the rails when the armature is at some position x as in (5) where w is the rail width, ρ_{rail} is the resistivity of the rail material, and v_c is the constant velocity[23]. For a linearly increasing velocity, v_c is one-half the instantaneous velocity v.

$$R_{rail}(t) = R'_{rail}\Delta x(t) \tag{4}$$

$$R_{vse} = \frac{1}{w}\sqrt{\frac{\rho_{rail}\mu_0}{\pi}}\sqrt{xv_c} \tag{5}$$

2.   Pulse Power Supply Modeling

Pulse power supplies (PPS) are often capacitor-based parallel-connected topologies in EML applications. Multiple PPS modules are used to excite the EMFY-3 launcher, each module having the schematic shown in Fig. 4. L_C and R_C represent equivalent series inductance (ESL) and equivalent series resistance (ESR) of the capacitors respectively. R_T and R_D are ON resistance of the thyristor and diode stacks. Pulse shaping inductor is per L_{PPS} with its ESR R_{PPS}. As each module's cable varies in length, they need to be modeled individually with their inductance and resistance, L_{cable}, and R_{cable} values. The PPS module model is shown in Fig. 6.
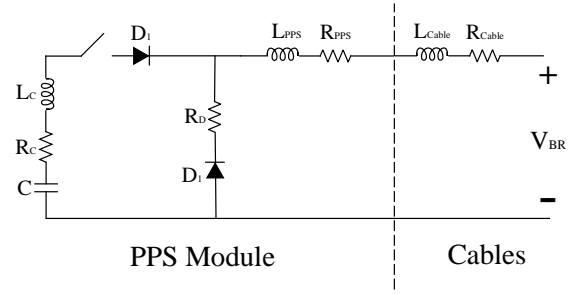

FIG. 6. The PPS module model.

3.   Kinemechanical Calculations

Propulsive force on the armature denoted as $\vec{F}_{pr}$ is calculated using propulsive inductance gradient, L'_{pr}, and rail current I_{rail} as in (1).

$$\vec{F}_{pr} = \frac{L'_{pr}I^2_{rail}}{2} \tag{6}$$

However, the $\vec{F}_{pr}$ is not the only force that acts on the armature. Friction and drag forces, denoted as $\vec{F}_{fric}$ and $\vec{F}_{drag}$ slow down the movement as in (7). $\vec{F}_{fric}$ can be modelled as in (8)[24] where μ_d and μ_s are dynamic and static friction coefficients respectively. ζ is the friction damping factor, and $\vec{F}_C$ is the contact force between the rails and the armature.

$$\vec{F}_{net} = max(0, \vec{F}_{pr} - \vec{F}_{fric} - \vec{F}_{drag}) \tag{7}$$

$$\vec{F}_{fric} = (\mu_d + (\mu_s - \mu_d)e^{\zeta v})\vec{F}_C \tag{8}$$

Aerodynamic drag can be modeled as in (9). C_d is the drag coefficient, A_{lp} is the area that frontier to the air, ρ_{air} is the density of air. There are no drag forces due to the eddy current in the containment as the EMFY-3 has a non-metallic containment.

$$\vec{F}_{drag} = \frac{1}{2}C_d A_{lp}\rho_{air}v^2_{arm} \tag{9}$$

Acceleration of the launch package can be expressed as in (10) where m_{lp} is the mass of the launch package. Other kinemechanical equations are presented from (11) to (14) where T_{exit} is the exit moment of the armature, X_{pre} is the pre-load position, and x_{rail} is the rail length.

$$\vec{F}_{net} = m_{lp}\vec{a}_{lp} \tag{10}$$

$$\vec{a}_{lp} = \frac{L'I^2_{rail}}{2m_{la}} \tag{11}$$

$$\vec{v}_{arm} = \int_0^{T_{exit}} \frac{L'I_{rail}^2}{2m_{la}} dt \tag{12}$$

$$\vec{x}_{arm} = \int_0^{T_{exit}} \int_0^{T_{exit}} \frac{L'I_{rail}^2}{2m_{la}} dt\,dt \tag{13}$$

$$x(0) = X_{pre} \quad x(T_{exit}) = x_{rail} \tag{14}$$

The model parameters of the kine-mechanical model are given in Table III. L'_{pr} is calculated 0.515 $\mu H/m$ from the 3-D FE model using (15) and (16) where V_{arm} denoted as the volume of the armature.

$$\vec{F}_{pr} = \iiint_{V_{arm}} \vec{J} \times \vec{B} \, dV \tag{15}$$

$$L'_{pr} = \frac{2F_{pr}}{I^2} \tag{16}$$

TABLE III. The Model Parameters.

Parameter	Value
C_d	1
A_{lp}	37.5 cm^2
ρ_{air}	1.225 kg/m^3
μ_d	0.3 [†]
μ_s	0.5 [†]
ζ	-0.01
X_{pre}	0.7 m

[†] μ_d, and μ_s are changing according to contact state.

B.   Control Method

The aforementioned control method where the proposed bus' inductance is not added is required to test the proposed model. In this subsection, features of the control method are discussed. Before the launch, the armature is located at the initial position called the pre-load distance. If the bus geometry is excluded, the EML uses geometry demonstrated in Fig. 7. Thus EML has an initial inductance denoted as L_0 can be calculated using L' as the L_0 is a portion of rails. The total inductance of the system can be rewritten as (17). Then, the initial inductance can be calculated (18), excluding any electromagnetic effect from its surroundings as the containment is non-conductive. Moreover, the module currents enter rails from the surface, although their cables are connected to buses at different locations. As module cables and their connections to the bus are not modeled implicitly, the complexity of the model is reduced.

$$L(t) = L'(x_{arm}(t) - X_{pre}) + L_0 \tag{17}$$
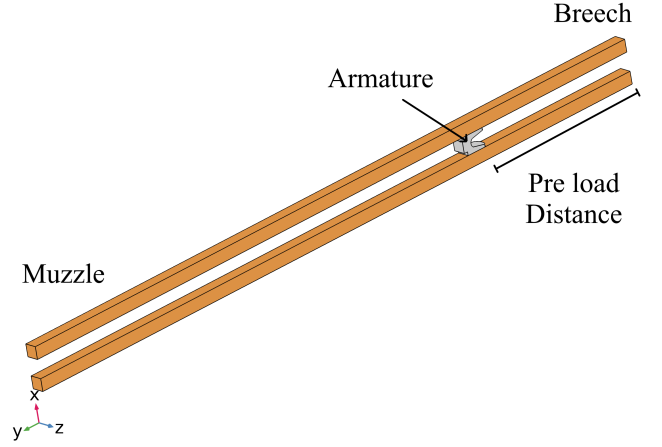
$$L_0 = X_{arm}L' \tag{18}$$

FIG. 7. The control method geometry.

C.   Proposed Method

Unlike the control method, the proposed method takes the effect of the bus geometry. Coaxial cables are connected to the bus according to their module number. Thus, if there is any interaction between the pre-load rail portion and bus geometry, 3-D FEM simulation should regard that aspect.

As each connection path introduces different has, so they should be added to the simulation model. The proposed model is illustrated in Fig. 8. L_1 and L_2 are used to model the difference in inductance paths. For example PPS_1 connected behind to the PPS_2 which can be seen in Fig. 9 and 10. For that reason, the PPS_1 current flows through $L_1 + L_2$, whereas PPS_2 current flows through just L_2.
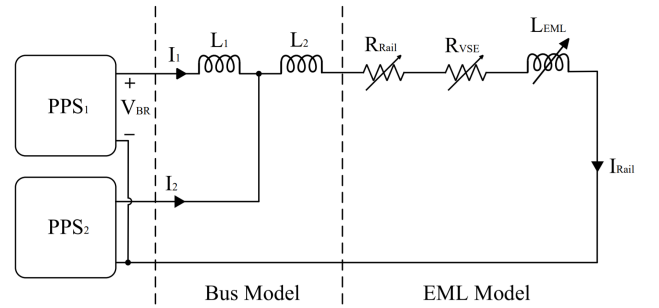

FIG. 8. The proposed EML model with separate bus inductances. Breech and muzzle points are located.

A FEM model is developed to investigate the impact of the bus geometry. In that regard, a test scenario is simulated in 3-D FEM. Two different cases are solved since the armature geometry movement is not allowed in 3-D electromagnetic FEM. The armature is located at the pre-load position in the first case, as in Fig. 7. The current density distribution and the magnetic field density vectors are demonstrated in Fig. 9. The result showed that the magnetic field distribution is disturbed due to the bus geometry. In the first phase of the launch (0-1
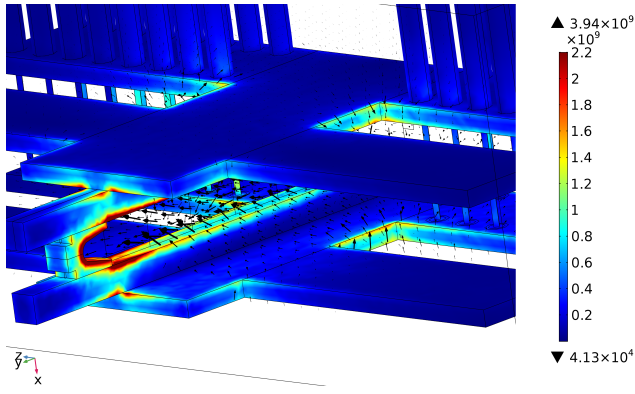
FIG. 9. Current density distribution and magnetic flux density vectors when the armature is located at its pre-load position. The color legend is for the current density only and its unit is A/m^2.
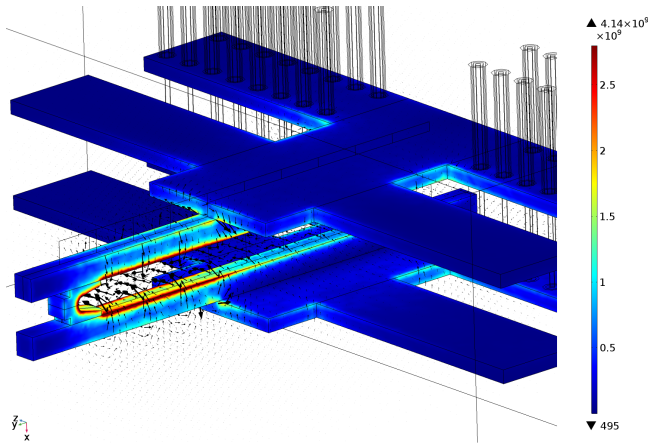

FIG. 10. Current density distribution and magnetic flux density vectors when the armature is located at ahead of its pre-load position. The color legend is for the current density only and its unit is A/m^2.

ms), the rail current changes, creating a time-varying magnetic field around the rails. These varying fields can not diffuse the bus geometry since it is conductive. Eddy currents in the bus not only create an additional loss but also reduce L_0 as they block the rail's magnetic field.

In the second phase, the armature moves from its pre-load position by 30 cm, and electromagnetic analysis is repeated. Current density distribution and the magnetic flux density vectors are illustrated in Fig. 10 can not be used to model L_0. L_0 should be decomposed into L_1 and L_2, and they are examined in 3-D FEM.

III.   METHODOLOGICAL DISCUSSION

The impacts of the geometric parameters are studied at in this section. A simple bus structure is demonstrated in Fig. 11 where w_{bus} represents the thickness of the bus, h_{bus} indicates the length in the launch direction, and l_{bus} is the length in the transverse direction. A parametric study is carried out to demonstrate the relationships between bus inductance and
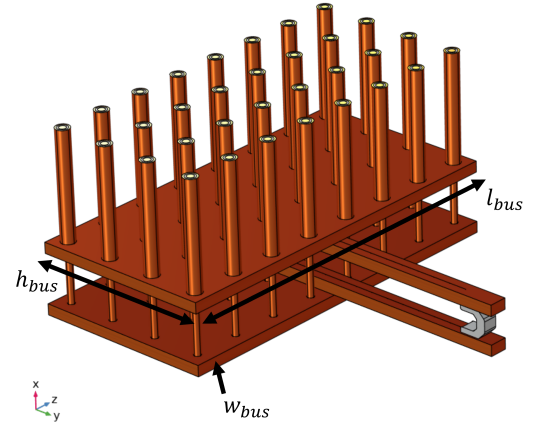

FIG. 11. The geometric parameters of the bus.

TABLE IV. The parametric study result. All PPS modules triggered at t = 0 to imitate the worst-case scenerio.

w_{bus} (m)	h_{bus} (m)	l_{bus} (m)	L'_{bus} (uH/m)	$F^{\dagger}$ (kN)
0.03	0.5	1.0	0.110	12.82
0.04	0.5	1.0	0.109	12.80
0.03	0.5	1.2	0.109	12.31
0.03	0.5	0.8	0.111	13.06
0.03	0.7	0.8	0.096	12.22
0.03	0.7	1.0	0.094	11.90
0.03	0.7	1.2	0.093	11.39
0.03	0.5	0.6	0.115	13.08

† Peak value. It is calculated using $F = \sqrt{F_y^2 + F_z^2}$.

its geometrical parameters. The results are shown in Table IV.

w_{bus} has the least influence on the inductance whereas l_{bus}, and h_{bus} have similar characteristic. The increase in the l_{bus}, and h_{bus} decreases the inductance as expected. However, the decrease is saturated since these dimensions are much larger than the rail cross-section. Lorentz forces between coaxial wires can be reduced by using a larger bus structure. However, a bigger bus entails higher costs and increased eddy current losses. Utilizing an H-shaped, or X-shaped bus can increase L'_{bus} since on average l_{bus} can be diminished.

Careful electromagnetic and mechanical simulations can be used to determine the ideal bus structure. Given certain mechanical restrictions, such as the mechanical stresses present in buses and cables, the bus geometry can be calculated considering a minimum mass/volume objective. However, this is not the scope of this paper.

IV.   RESULTS

This section compares experimental findings to the proposed model, which includes bus impact, and the control method, which does not. 20 launch tests with the EMFY-3 launcher were conducted in all, but only three of them are

shared in the article. The control method establishes a benchmark, whereas the proposed method focuses on improvements.

The ability to obtain high accuracy measurements is crucial for comprehending the underlying physics and solving these issues. Thus, several instruments are installed at ASELSAN EM launch laboratory, which is presented in detail in one of the previous articles[10]. B-dot probes positioned close to the rails are used to track the projectile's movement. Although this method is accepted as a standard method for determining a projectile's kinetic state variables, considerable inaccuracies may occur because of strong electromagnetic radiation or shock waves generated by a projectile traveling at a high speed. Moreover, it has inherent quantization error since a few sensors can be employed on the rails. In order to enhance the measurements from B-dot sensors, a Doppler velocity radar system is used. This system is also non-invasive and robust to harsh operation conditions, unlike B-dots. It has higher resolution and lesser quantization error. Furthermore, the muzzle velocity is also measured with high-speed (Hi-FPS) cameras. Measurement errors of any kind are attempted to be mitigated by using multiple instruments. Nevertheless, all three instruments have a measurement problem at the beginning of the launch, velocities lower than 50 m/s. This does not create a drastic error in kine-mechanical calculations if the friction is modeled successfully.

Rogowski coils are utilized for current measurements. The rail current is measured by employing a coil around the bus. Each PPS module current is also measured. The sum of each PPS module current should be equal to the rail current due to Kirchoff Current Law (KCL). Any kind of current measurement error, e.g. a misalignment of coils, can be detected simply by checking whether KCL holds or not. Breech and muzzle voltage measurements are taken by differential voltage probes. The most challenging diagnostics is the muzzle voltage measurement, peers report several articles to understand its physical origin[25]. Nevertheless, these measurements are mostly related to the state of the electrical contact. Thus, they are not directly related with launch simulations. It is often assumed to have healthy contact between rails and the armature, so these measurements do not create drastic effects on model correction studies.

As aforementioned, the aim is to create pulse shape rail current; thus, the triggering times are evaluated accordingly. Since these calculations are made with the control method, unexpected deviations occurred at the rail current waveforms. Three of them are illustrated in Fig. 12 with their expected reference levels. Test parameters of these launches are demonstrated in Table V. At the initial state (0-1ms), rail currents overshot from their reference value, resulting in larger peak currents. This phenomenon occurred dominantly with larger rail currents.

The simulation results of the control method, proposed method, experimental results, and improvement ratios (IR) are given in Table VI. The improvement ratio used to compare the two methods uses mean absolute error (MAE) measurements such as armature exit time, muzzle current, and muzzle speed. MAE and the IR are defined in (19) and (20) respectively
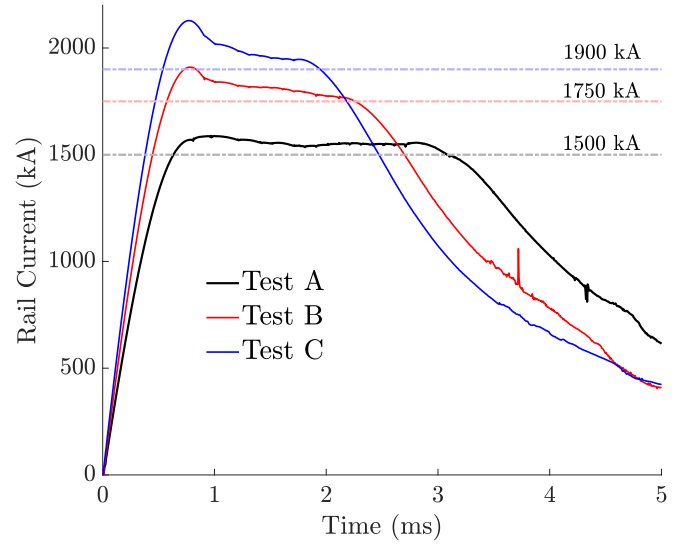

FIG. 12. Rail current measurements. Reference currents are indicated with dashed lines.

where $\hat{x}_{control}$, $\hat{x}_{proposed}$ and x denote the simulated value of control method, the simulated value of the proposed method, and experimental result.

TABLE V. Test Parameters

	Peak Rail Current	PPS Energy
Test A	1.58 MA	8 MJ
Test B	1.91 MA	8 MJ
Test C	2.12 MA	8 MJ

$$MAE = |\hat{x} - x| \tag{19}$$

$$IR = \frac{MAE(\hat{x}_{control}, x) - MAE(\hat{x}_{proposed}, x)}{x} \tag{20}$$

The simulated and experimental rail current waveforms and breech voltages are demonstrated for comparison in Fig. 13-15. Turquoise color is used to demonstrate the improved region. The peak current and the breech voltage waveform are improved in terms of accuracy in the improved region. As the bus impact will be diminished when the rail current is in DC, findings are consistent with theory. In Fig. 16, the simulated and experimental velocity curves are illustrated with three launches. The proposed method gives more consistent findings, whereas the control method underestimates the muzzle velocity. As both methods use the same kine-mechanical equations, and L'_{pr}, the difference occurs due to rail current calculation errors. These errors are dependent on the inductance variation of the EML. Thus, the proposed model provides more accurate results than the control method. Peak rail currents and muzzle energies calculations improved by 5.71% and 2.40% on average.

TABLE VI. Some Critical Outputs of the EMFY-3 Experiments and Simulations with the control and proposed methods.

	P.M.	C.M.	Exp.	Improvement[1]
Test A				
Peak Rail Current	1.56 MA	1.51 MA	1.59 MA	5.28%
Muzzle Current	0.80 MA	0.78 MA	0.81 MA	3.50%
Muzzle Velocity	2241 m/s	2186 m/s	2238 m/s	2.32%
Test B				
Peak Rail Current	1.86 MA	1.75 MA	1.91 MA	5.65%
Muzzle Current	0.76 MA	0.74 MA	0.75 MA	1.12%
Muzzle Velocity	2354 m/s	2290 m/s	2312 m/s	-0.86%
Test C				
Peak Rail Current	2.07 MA	1.94 MA	2.13 MA	6.20%
Muzzle Current	0.75 MA	0.70 MA	0.74 MA	4.85%
Muzzle Velocity	2428 m/s	2357 m/s	2418 m/s	2.11%

[1] Improvement ratio is described at (20).

FIG. 14. Simulation and experimental results for the rail currents and breech voltages. Test B.

FIG. 13. Simulation and experimental results for the rail currents and breech voltages. Test A.
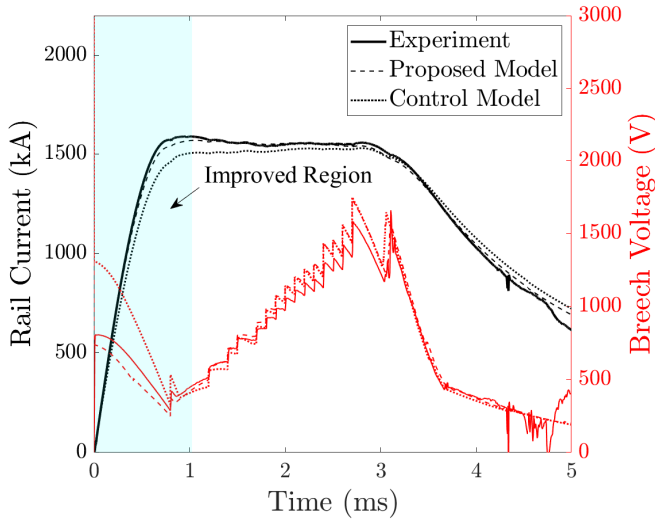

FIG. 15. Simulation and experimental results for the rail currents and breech voltages. Test C.

V. DISCUSSION

The aim of this article is to investigate the importance of accurate calculation of bus inductance on overall inductance distribution. The bus structure reduces the rail inductance by almost half. An important implication can be found considering the armature pre-load distance. For example, if the armature is located inside or near the bus structure, its acceleration can be reduced. Because reduction in rail inductance also reflects the propulsive force. However, putting the armature way after the bus structure also reduces the effective rail length. This results in a reduction in the muzzle velocity. However, the optimum position of the armature is not in the scope of this paper. Future work can be extended considering these facts.
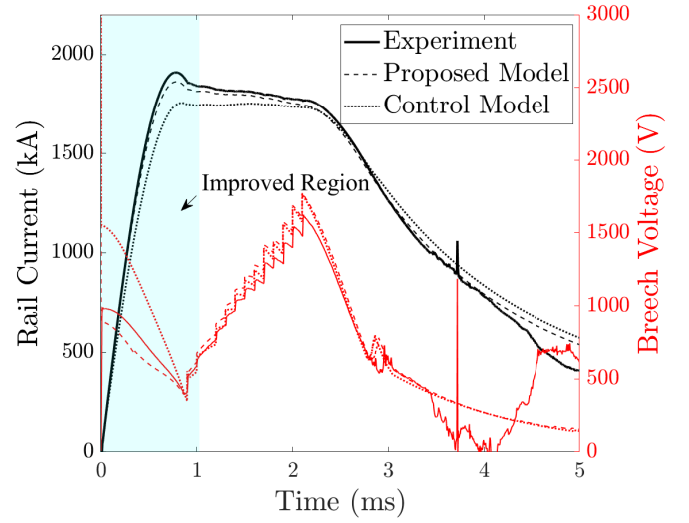
VI. CONCLUSIONS

The remarks obtained throughout the development of the simulation model and conducted experimental results can be listed as follows.

1. The proposed model improves the simulation accuracy, especially at the peak rail current. This is particularly crucial for large-caliber EMLs.

2. The bus geometry affects the magnetic field distribution around the rail portion, which intersects. The lack of magnetic field diffusion reduces the related inductance, which increases the peak rail current. The bus impact is dominant in the first phase of the launch, where the rail current is transient.
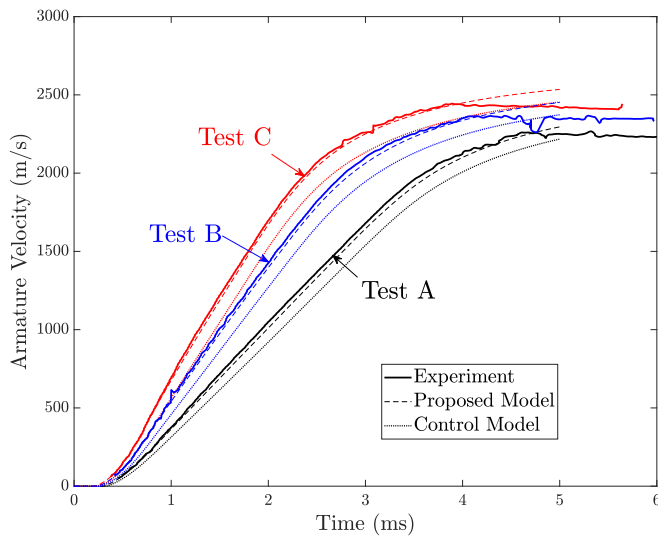
FIG. 16. Simulation and experimental results for the velocity curves.

3. L_0 can not be modeled as in (18) when PPS is connected with large buses. A detailed electromagnetic 3-D FEM is required to calculate.

4. When multiple PPS are used to excite one EML, every inductance path is important and should be analyzed. The proposed model can be useful for distributed energy supply (DES) to excite long EMLs.

5. Pre-load distance is an important parameter when a large bus structure is utilized. The bus structure not only reduces the inductance of the EML but also decreases the propulsive force at the start. As the armature acceleration is caused by spatial inductance variation, lowering the initial inductance reduces the propulsive force. The bulk copper acts like an eddy brake.

ACKNOWLEDGMENTS

[1] N. Tosun, A. Civil, A. Y. Oruç, B. Yildirim, B. M. Özceylan, B. Bolat, E. B. Yurdakul, E. Tan, F. Yurdakonar, H. Akdemir, Güngen, Önür, M. Karagöz, Cavbozar, R. H. Demirkol, U. Göçmen, and O. Keysan, "Sensitivity analysis for the inductance gradient of emfy-3 electromagnetic launcher," IEEE Transactions on Plasma Science , 1–6 (2022).

[2] M. Karagoz, Y. Çevik, E. Tan, A. Civil, O. Cavbozar, U. Gocmen, B. Yildirim, E. Durna, and M. Sahin, "Aselsan emfy-1 electromagnetic launcher: First experiments," in *2017 IEEE 21st International Conference on Pulsed Power (PPC)* (2017) pp. 1–3.

[3] H. Zhang, G. Cheng, W. Guo, Z. Su, and T. Zhang, "A lumped parameter model and its code for capacitor-based railgun with arbitrary number of pfus," IEEE Trans. Plasma Sci. **42**, 2098–2103 (2014).

[4] H. Zhang, G. Cheng, W. Guo, Z. Su, T. Zhang, and Y. Yang, "Calculating timing sequence of capacitor-based railgun with given muzzle velocity," IEEE Trans. Plasma Sci. **43**, 3298–3303 (2015).

[5] N. Tosun, H. Polat, and O. Keysan, "Electromagnetic launcher speed control with a multilevel fast triggering time algorithm (mftta)," in *2021 IEEE Pulsed Power Conference (PPC)* (2021) pp. 1–10.

[6] F. Deadrick, R. Hawke, and J. Scudder, "Magrac–a railgun simulation program," IEEE Trans. Magn. **18**, 94–104 (1982).

[7] G. E. Rolader, L. D. Thornhill, J. H. Batteh, and J. J. Scanlon, "Electromagnetic gun circuit analysis code (egcac)," IEEE Trans. Magn. **29**, 499–504 (1993).

[8] J. Wey, E. Spahn, and M. Lichtenberger, "Railgun modeling with the p-spice code," IEEE Trans. Magn. **33**, 619–624 (1997).

[9] N. Tosun, *Transient Modeling Techniques for the Analysis of Electromagnetic Launchers*, Master's thesis, Middle East Technical University (2021).

[10] M. Karagoz, A. Civil, B. Yildirim, E. B. Yurdakul, E. Durna, E. Tan, O. Cavbozar, U. Gocmen, and Y. Cevik, "Aselsan electromagnetic launch laboratory: First shot," IEEE Transactions on Plasma Science **48**, 802–807 (2020).

[11] S. Tan, J. Lu, B. Li, Y. Zhang, and Y. Jiang, "A new finite-element method to deal with motion problem of electromagnetic rail launcher," IEEE Trans. Plasma Sci. **45**, 1374–1379 (2017).

[12] K. . Hsieh and V. Thiagarajan, "A novel split-domain iteration scheme for solution of electromagnetic diffusion problems modeled by the hybrid finite-element–boundary-element formulation," IEEE Trans. Magn. **45**, 587–590 (2009).

[13] P. Zuo, Y. Geng, J. Li, and J. Yuan, "An approach for eddy-current calculation in railguns based on the finite-element method," IEEE Trans. Plasma Sci. **43**, 1592–1596 (2015).

[14] Q. hua Lin and B. ming Li, "Numerical simulation of interior ballistic process of railgun based on the multi-field coupled model," Defence Technology **12**, 101 – 105 (2016), 2016 International Symposium on Ballistics.

[15] D. Ceylan, M. Karagöz, Y. Çevik, B. Yıldırım, H. Polat, and O. Keysan, "Simulations and experiments of emfy-1 electromagnetic launcher," IEEE Transactions on Plasma Science **47**, 3336–3343 (2019).

[16] N. Tosun, H. Polat, D. Ceylan, M. Karagoz, B. Yıldırım, Güngen, and O. Keysan, "A hybrid simulation model for electromagnetic launchers including the transient inductance and electromotive force," IEEE Transactions on Plasma Science **48**, 3220–3228 (2020).

[17] N. Tosun, D. Ceylan, H. Polat, and O. Keysan, "A comparison of velocity skin effect modeling with 2-d transient and 3-d quasi-transient finite element methods," IEEE Transactions on Plasma Science **49**, 1500–1507 (2021).

[18] S. Satapathy and H. Vanicek, "Down-slope contact transition in railguns," IEEE Transactions on Magnetics **43**, 402–407 (2007).

[19] M. S. Bayati, A. Keshtkar, and A. Keshtkar, "Transition study of current distribution and maximum current density in railgun by 3-d fem–iem," IEEE Transactions on Plasma Science **39**, 13–17 (2011).

[20] J. V. Parker and S. Levinson, "Loss of propulsive force in railguns with laminated containment," IEEE Transactions on Magnetics **35**, 442–446 (1999).

[21] D. Landen and S. Satapathy, "Eddy current effects in the laminated containment structure of railguns," IEEE Transactions on Magnetics **43**, 150–156 (2007).

[22] J. Mallick, "Phenomenological electromagnetic modeling of laminated-containment launchers," IEEE Transactions on Magnetics **43**, 359–363 (2007).

[23] T. G. Engel, J. M. Neri, and M. J. Veracka, "Characterization of the velocity skin effect in the surface layer of a railgun sliding contact," IEEE Transactions on Magnetics **44**, 1837–1844 (2008).

[24] J. Wu, G. Wan, N. Cheng, L. Li, and B. Li, "Research on armature's wearing and dynamic interior ballistic of a railgun," IEEE Transactions on Plasma Science **45**, 1202–1207 (2017).

[25] Y. Dreizin and J. Barber, "On the origins of muzzle voltage," IEEE Transactions on Magnetics **31**, 582–586 (1995).